Brief Papers

Steering a Ferromagnetic Particle by Optimal Magnetic Feedback Control

Arash Komaee, *Member, IEEE*, and Benjamin Shapiro

***Abstract*—A class of feedback control policies for steering a magnetic particle in a viscous fluid and actuated by a magnetic field is presented. The magnetic field which is generated by an array of electromagnets can be adequately shaped by controlling the voltages of the electromagnets. Control design relies on a dynamical model which exploits the low-pass character of the electromagnets, the opposing viscous drag on the magnetic particle, and the nonlinear (quadratic) nature of the dependence of the magnetic force on the electrical currents passing through the electromagnets. It is shown that under a set of practically achievable conditions, the nonlinearity of the model can be canceled by incorporating an inverse nonlinear map in the controller so that the closed-loop system operates like a linear system. A systematic framework for determining an optimal inverse map and investigating its properties is developed and two important cases of minimum control effort and maximum robustness are discussed. The ability to control the magnetic particle along arbitrary trajectories is verified both in simulations and in an experiment.**

***Index Terms*—Magnetic feedback control, nonlinear system, optimal control, quadratic nonlinearity, trajectory tracking.**

I. Introduction

We consider the design, implementation, and verification of a class of feedback control policies for steering a magnetic particle (or a drop of a ferromagnetic fluid) along arbitrary trajectories in a controlled magnetic field. Applications of this control problem include magnetic tweezers [1]–[4], lab-on-a-chip systems that include magnetic particles or fluids [5], [6], and magnetofection [7].

The controlled magnetic field which actuates the magnetic particle is generated by an arrangement of electromagnets. The set of voltages of these electromagnets represents a control vector. The control design problem is to determine this control vector in terms of the position of the magnetic particle (current position and possibly its history) such that the resulting magnetic force drives the particle along any desired trajectory. The magnetic force is a highly nonlinear function of both position and control vector; it sharply drops with distance from the electromagnets and depends quadratically on the control vector. Our control design is based on the finding that the quadratic structure of this function allows for a nonlinear transformation of the control vector so that the magnetic force can be freely assigned. Considering that the magnetic particle moves inside a surrounding fluid, its motion is influenced by an opposing drag force which according to Stokes' drag law [8], [9] is linear in the velocity of the particle. Thus, we conclude from Newton's second law that the dynamics of the magnetic particle is governed by a linear model whose input vector is the magnetic force which now can be freely assigned. In summary, application of the nonlinear transformation converts the original problem to the much easier problem of linear controller design.

The nonlinear transformation is a mapping from the set of all magnetic force vectors into a subset of the control vectors. As this mapping is not unique, we first determine a parametric expression representing the infinite set of all admissible mappings, and then we choose among this set the mapping which is optimal in some appropriate sense. We consider two specific optimality criteria: minimum control effort (minimum control vector magnitude) and maximum robustness against modeling errors.

Compared to prior results in magnetic control [2], [10]–[12], our control strategy exploits the nonlinear nature of the system, it accounts for the dynamics of the electromagnets, it allows us to exactly achieve any desired magnetic force at any location, and it is optimal in a desirable sense. Creighton *et al.* addressed a similar magnetic control problem in [13], [14]. Beyond this, and beyond our prior results [15], [16], this paper includes model uncertainty, a robust control policy and subsequent analysis of the minimum effort control, an extension of our approach to three dimensions (the results of [15] were restricted to the planar case), and the introduction of a nonlinear filtering scheme to handle spatial discontinuities in the optimal nonlinear transformation.

II. Model

We present a dynamical model to describe the motion of a magnetic particle (or a single drop of ferrofluid held together by surface tension) in a surrounding fluid under a controlled magnetic field and opposing drag forces. The motion of the particle can be confined to a plane ($m = 2$) or the particle can be free to move in a three-dimensional space ($m = 3$).

Let $\mathscr{C}$ be a bounded domain in $\mathbb{R}^m$ and assume that a magnetic field is present over $\mathscr{C}$ due to $n \geqslant 2m$ electromagnets which are located outside of $\mathscr{C}$. Let $i_k(t)$ denote the electrical current of the k^{th} electromagnet as a function of time t and assume that the electromagnets operate in their linear regime such

Manuscript received August 17, 2010; revised February 04, 2011; accepted April 11, 2011. Manuscript received in final form May 03, 2011. Date of publication June 30, 2011; date of current version May 22, 2012. Recommended by Associate Editor A. Serrani. This work was supported by the National Institutes of Health under Grant R21EB009265.

A. Komaee is with the Department of Aerospace Engineering, University of Maryland, College Park, MD 20742 USA (e-mail: akomaee@umd.edu).

B. Shapiro is with the Fischell Department of Bio-Engineering and the Institute for Systems Research, University of Maryland, College Park, MD 20742 USA (e-mail: benshap@eng.umd.edu).

Digital Object Identifier 10.1109/TCST.2011.2152842

that the magnetic field generated by each electromagnet is linearly related to its current.[1] This implies that the magnetic field due to electromagnet k can be expressed as $i_k(t)h_k(r)$, where the vector field $h_k(r) \in \mathbb{R}^m$ is the magnetic field at a point $r = [r_1 \cdots r_m]^T \in \mathscr{C}$ generated by electromagnet k due to a unit electrical current. This vector field is formed by solving Maxwell's equations [17]. The linearity of Maxwell's equations implies that the total magnetic field at a point $r \in \mathscr{C}$ is given by

$$h(r,t) = \sum_{k=1}^{n} i_k(t)h_k(r). \tag{1}$$

A special case of interest is when $\mathscr{C}$ is a circle $(m = 2)$ with a radius a centered at the origin of the coordinate system and the electromagnets are identical and are placed equally distanced around the circle. Let $h_c(r)$ be the magnetic field around a single magnet placed at the origin of a coordinate system and pointing to the right. Then $h_k(r)$, $k = 1, 2, \ldots, n$ can be written using translations and rotations as

$$h_k(r) = -C_k^T h_c(ae - C_k r) \tag{2}$$

where $e = [1 \quad 0]^T$ and the rotation matrix C_k is given by

$$C_k = \begin{bmatrix} \cos(2\pi(k-1)/n) & \sin(2\pi(k-1)/n) \\ -\sin(2\pi(k-1)/n) & \cos(2\pi(k-1)/n) \end{bmatrix}.$$

Let L be a $n \times n$ symmetric constant matrix whose diagonal elements L_{kk} are the self inductance of electromagnet k and whose off-diagonal elements $L_{jk} = L_{kj}$ are the mutual inductance between electromagnets j and k. Suppose that R_k is the internal resistance of electromagnet k and define the diagonal matrix $R = \mathrm{diag}(R_1, R_2, \ldots, R_n)$. Assume that $u_k(t)$ is the voltage of electromagnet k and set $y_k(t) = R_k i_k(t)$; then define the control vector $u = [u_1 \quad u_2 \quad \cdots \quad u_n]^T$ and the state vector $y = [y_1 \quad y_2 \quad \cdots \quad y_n]^T$. Note that the magnetic flux associated with electromagnet k is given by the sum $\phi_k = \sum_{j=1}^{n} L_{kj} i_j$ and Ohm's law [18] implies that $i_k = (u_k - \dot{\phi}_k)/R_k$. These two equalities lead to the state-space equations

$$\begin{aligned} \dot{y}(t) &= -RL^{-1}y(t) + RL^{-1}u(t) \\ i(t) &= R^{-1}y(t) \end{aligned} \tag{3}$$

where $i = [i_1 \quad i_2 \quad \cdots \quad i_n]^T$ is the vector of electrical currents.

For simplicity of notation, (3) is rewritten as

$$\dot{y}(t) = -\sigma_s A y(t) + \sigma_s A u(t) \tag{4}$$

where σ_s is the smallest eigenvalue of RL^{-1} and A is defined as $A = RL^{-1}/\sigma_s$. The advantage of this representation is that under the reasonable assumptions that the electromagnets are identical and their mutual inductance is negligible, A is the identity matrix. For simplicity of notation in the next steps, we also define $\Omega = R^* R^{-1}$, where $R^* = \max\{R_1, R_2, \ldots, R_n\}$.

The magnetic force applied to a ferromagnetic particle due to the magnetic field (1) is given by

$$f_{\mathrm{mag}}(r,t) = k_u \nabla \|h(r,t)\|^2 \tag{5}$$

where $\|\cdot\|$ is the Euclidean norm, the operator ∇ denotes the gradient with respect to r, and $k_u > 0$ is a known constant depending on the volume of the particle and its permeability [9], [19]. In order to determine a compact expression for the magnetic force, the magnetic field (1) is represented in matrix form as

$$h(r,t) = H(r)y(t) \tag{6}$$

where the $m \times n$ matrix $H(r)$ is defined as

$$H(r) = \frac{1}{R^*}\,[\,h_1(r) \quad h_2(r) \quad \cdots \quad h_n(r)\,]\,\Omega.$$

Substituting (6) into (5), we can write

$$f_{\mathrm{mag}}(r,t) = k_u g(r, y(t)) \tag{7}$$

where the mapping $g(\cdot) : \mathbb{R}^m \times \mathbb{R}^n \to \mathbb{R}^m$ is given by

$$\begin{aligned} g(r,y) &= \nabla \|H(r)y\|^2 \\ &= 2\left[\frac{\partial (H(r)y)}{\partial r}\right]^T H(r)y. \end{aligned} \tag{8}$$

Here, $\partial(H(r)y)/\partial r$ denotes the Jacobian matrix of the vector $H(r)y$ with respect to r.

The magnetic particle accelerates inside a viscous fluid under the influence of three forces: the magnetic force (7), the fluid resistance (drag) $f_{\mathrm{drag}}(t)$, and any disturbances $f_{\mathrm{dist}}(t)$. Stokes' drag law [8], [9] states that the drag force is linear in the velocity vector $v(t) = \dot{r}(t)$, i.e.,

$$f_{\mathrm{drag}}(t) = -\mu v(t). \tag{9}$$

Here, $\mu > 0$ is a known constant which depends linearly on the diameter of a spherical particle (or on the properties of the nano-particles in the ferrofluid droplet) and the viscosity of the surrounding fluid [8], [9], [16].

Newton's second law of motion states that

$$m_p \dot{v}(t) = f_{\mathrm{mag}}(r,t) + f_{\mathrm{drag}}(t) + f_{\mathrm{dist}}(t)$$

where m_p is the mass of the particle. Substituting (7) and (9) into this equation, we get

$$\dot{v}(t) = -\sigma_v v(t) + \sigma_v k_g g(r(t), y(t)) + \sigma_v d(t) \tag{10}$$

where $\sigma_v = \mu/m_p$, $k_g = k_u/\mu$, and $d(t) = f_{\mathrm{dist}}(t)/\mu$.

We combine (4), (10), and $\dot{r} = v$ to describe the complete dynamics of the system as

$$\dot{y}(t) = -\sigma_s A y(t) + \sigma_s A u(t) \tag{11a}$$

$$\dot{r}(t) = v(t) \tag{11b}$$

$$\dot{v}(t) = -\sigma_v v(t) + \sigma_v k_g g\,(r(t), y(t)) + \sigma_v d(t) \tag{11c}$$

[1] As a consequence of Biot-Savart law [17], an air core solenoid is always linear. An iron core solenoid is approximately linear below its core saturation magnetization [17].

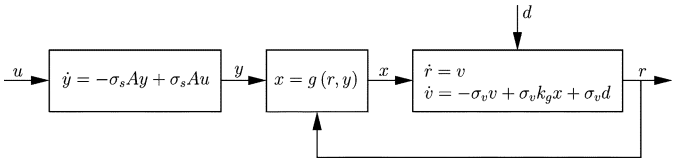

Fig. 1. Block diagram of the system consists of a cascade combination of two linear dynamical systems and a memoryless nonlinear system.

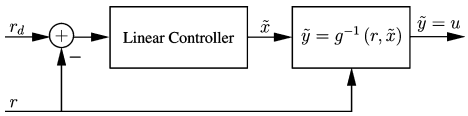

Fig. 2. Structure of a nonlinear controller under the assumption that the electromagnet dynamics is fast such that $y \simeq u$.

with the $(n + 2m)$-dimensional state vector (y, r, v), the control input u, and the disturbance vector d. Note that the nonlinear system in (11) can be represented as a cascade combination of the linear dynamical system (11a) with the memoryless nonlinear system

$$x(t) = g(r(t), y(t))$$

followed by the linear dynamical system

$$\begin{aligned} \dot{r}(t) &= v(t) \\ \dot{v}(t) &= -\sigma_v v(t) + \sigma_v k_g x(t) + \sigma_v d(t). \end{aligned} \tag{12}$$

This representation is illustrated in the block diagram of Fig. 1.

We close this section by noting a practical condition for the validity of the state-space model (11). In experiments, the applied electromagnet voltages u_k are limited by the maximum voltage $u_{\max}$ which can be provided by the drivers (voltage sources) of the electromagnets. To keep the model in its range of validity, we thus impose the condition $|u_k| \leqslant u_{\max}$ on all elements of the control vector.

III. Controller Design

The desired controller, in the most general case, is a map from $\{r(\tau), 0 \leqslant \tau \leqslant t\}$ into $u(t)$ which properly manipulates the magnetic field such that the particle tracks any desired trajectory $r_d(t)$. We shall assume that the position vector $r(t)$ is measured by an appropriate sensor such as a high resolution camera. In practice, the measurement precision is limited by the finite resolution of the camera, noise, and other sources of error. Thus, the actual output of the measuring device is the position vector $r(t)$ impaired by an additive measurement noise. For the purpose of controller design, we disregard this measurement noise as well as the disturbance vector $d(t)$ in (11). Once the design is completed, the effect of measurement noise and disturbance can be examined by means of analytical or numerical methods.

It is shown in Section IV that there exists an inverse map $g^{-1}(\cdot) : \mathbb{R}^m \times \mathbb{R}^m \to \mathbb{R}^n$ such that

$$g(r, g^{-1}(r, x)) = x \tag{13}$$

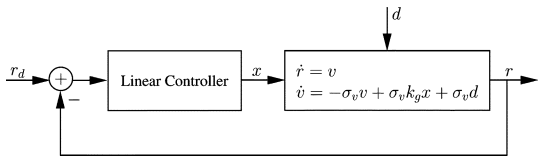

Fig. 3. Linear equivalent of the closed-loop system.

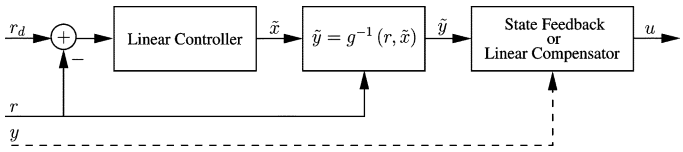

Fig. 4. Structure of a nonlinear controller with compensation for the bandwidth of the subsystem (11a).

for every r and x. For the sake of simplicity, we first consider the case where the inductance dynamics (11a) (the first block of Fig. 1) is much faster than the closed-loop dynamics. Since the linear subsystem (11a) has a unit gain, this condition allows us to approximate its output with its input, i.e., $y(t) \simeq u(t)$. Under this assumption, we propose a nonlinear controller with the structure illustrated in Fig. 2. This controller consists of a linear controller followed by the inverse map $g^{-1}(\cdot)$ defined in (13). Based on the assumption of $y(t) \simeq u(t)$, we can drop the first block of the system in Fig. 1. Therefore, upon connecting the controller to the system, the nonlinear blocks of the controller and the system will be in cascade and according to (13) will cancel each other, i.e., $x = \tilde{x}$. This equality simplifies the entire closed-loop system to the linear system of Fig. 3. The problem of controller design for this linear system is a straightforward problem of linear control theory [20]–[22]. In the literature of nonlinear control, this method of converting a nonlinear system to a linear system is referred to as exact feedback linearization, see for example [23], [24]. For this specific problem, application of the inverse map leads to both input-state and input-output linearization.

After designing the linear controller in Fig. 3, the bandwidth BW of the closed-loop system is known and we can check for the validity of the approximation $y(t) \simeq u(t)$. For this approximation to be valid, it is necessary that the input $u(t)$ passes through the linear system (11a) with a small distortion, which means that the bandwidth BW^* of $u(t)$ must be significantly smaller than the bandwidth σ_s of (11a). On the other hand, BW^* can be determined in terms of BW by noting that $\tilde{x}(t)$ has a bandwidth of BW and $u(t)$ is generated by passing this signal through the nonlinear inverse map $g^{-1}(\cdot)$. We suppose that BW^* should be several times larger than BW as a result of nonlinearity of the inverse map.

For the case when $\sigma_s \gg BW^*$ is not satisfied, we can increase the bandwidth of (11a) using a state feedback (if the observation of $y(t)$ is available) or an open-loop linear compensator. For this purpose, the output of the controller in Fig. 2 is passed through a linear compensator before being applied to the system of Fig. 1. This approach is illustrated in Fig. 4.

When the observation of $y(t)$ via measuring the electrical currents of the electromagnets is provided to the controller, the last block of Fig. 4 can be characterized by the linear state feedback

$$u(t) = y(t) + \frac{\sigma_s^*}{\sigma_s}(\tilde{y}(t) - y(t))$$

where σ_s^* is a constant satisfying $\sigma_s^* \gg BW^*$. This control leads to the state-space equation

$$\dot{y}(t) = -\sigma_s^* A y(t) + \sigma_s^* A \tilde{y}(t) \tag{14}$$

which has the same form of (11a), albeit with an acceptable bandwidth. If due to technical or cost limitations the electrical currents cannot be measured and the observation of $y(t)$ does not exist, the compensator block can be filled with the linear dynamical system

$$\dot{\hat{y}}(t) = -\sigma_s^* A \hat{y}(t) + \sigma_s^* A \tilde{y}(t)$$
$$u(t) = \hat{y}(t) + \frac{\sigma_s^*}{\sigma_s}(\tilde{y}(t) - \hat{y}(t)).$$

For $u(t)$ determined from this compensator, it is straightforward to show that $y(t) - \hat{y}(t) \to 0$ as $t \to \infty$, which means that $y(t)$ asymptotically $(t \to \infty)$ satisfies (14).

In designing the linear controller block in Figs. 2 and 4, it must be taken into consideration that the generated control $u(t)$ must be subject to the constraint $\|u(t)\|_\infty \leqslant u_{\max}$. While we choose the control parameters such that the control vector will remain below this level in a normal mode of operation, this condition may occasionally be violated if the reference signal $r_d(t)$ changes very quickly. A trivial fix is to cap the elements $u_k(t)$ of the control vector by $\pm u_{\max}$ but this is not the best solution to the problem since it causes significant error in the direction of the vector $x(t)$ in Fig. 3. An appropriate alternative [25], [26] is to modify $u(t)$ by multiplying it with a gain

$$k_{\mathrm{Lim}}(t) = \begin{cases} 1, & \|u(t)\|_\infty \leqslant u_{\max} \\ \dfrac{u_{\max}}{\|u(t)\|_\infty}, & \|u(t)\|_\infty > u_{\max}. \end{cases}$$

The advantage of this modification is that it only changes the amplitude of $x(t)$ but not its direction.

The main task of this paper, determining the inverse map $g^{-1}(\cdot)$, will be addressed in Section IV. Also, we shall explain that certain smoothness limitations of $g^{-1}(\cdot)$ require slight modifications of the controller structure proposed in this section.

IV. Inverse Map

In order to determine the inverse map $y = g^{-1}(r, x)$ defined in (13), we need to solve the algebraic equation

$$g(r, y) = x \tag{15}$$

with respect to y for fixed but arbitrary values of r and x. Since the number of equations in (15) is smaller than the number of unknowns (m versus $n \geqslant 2m$), if there exists a solution for the equations, this solution is not necessarily unique. Therefore, our task is to obtain among all possible solutions of (15) the solution which optimizes a desired metric. This metric can be chosen to achieve the minimum control effort (the solution of (15) with the minimum Euclidean norm) or the maximum robustness against variations in the model parameters.

We solve this optimization problem in two steps: first, a parametric family of solutions of (15) is determined in terms of a parameter vector in $\mathbb{R}^{n-2}$, and then, the desired metric is optimized with respect to this parameter vector. The advantage of this method is that optimization with respect to $n-3$ parameters has a closed form solution, and so only one parameter requires numerical optimization. In the following two subsections, we focus our attention on these two steps for the case of $m = 2$. Then, in Subsection IV-C, we extend our approach and results to the three-dimensional space $(m = 3)$.

A. Parametric Family of Solutions

In order to determine a parametric solution for (15), we consider the explicit expression (8) for $g(\cdot)$ and substitute

$$H(r)y = p \tag{16}$$

into this expression. This substitution leads to

$$2\left[\frac{\partial(H(r)y)}{\partial r}\right]^T p = 2\left[\frac{\partial\left(H^T(r)p\right)}{\partial r}\right]^T y = x$$

where the first equality on the left is concluded from differentiating both sides of $p^T H(r)y = y^T H^T(r)p$ with respect to r. Combining this equation with (16), we get

$$\begin{bmatrix} H(r) \\ \left(\dfrac{\partial\left(H^T(r)p\right)}{\partial r}\right)^T \end{bmatrix} y = \begin{bmatrix} p \\ \frac{1}{2}x \end{bmatrix} \tag{17}$$

which is a linear equation with respect to y for every fixed value of the parameter vector p. Suppose that $m = 2$ and let (ρ, ϕ) be the polar representation of p, i.e.,

$$p = \rho\,[\cos\phi \quad \sin\phi]^T$$

where $\rho \geqslant 0$ and $\phi \in [0, 2\pi)$. Then, substituting this representation into (17) and left multiplying the equation by an appropriate nonsingular matrix, it can be written as the linear equation

$$F(\phi)H_e(r)y = \rho e + \frac{1}{\rho}Ex \tag{18}$$

where $e = [1 \quad 0 \quad 0 \quad 0]^T$, $E = [0_{2\times 2} \quad \frac{1}{2}I_2]^T$

$$F(\phi) = \begin{bmatrix} \cos\phi & \sin\phi & 0 & 0 & 0 \\ -\sin\phi & \cos\phi & 0 & 0 & 0 \\ 0 & 0 & \cos\phi & \sin\phi & 0 \\ 0 & 0 & 0 & \cos\phi & \sin\phi \end{bmatrix}$$

and the $5 \times n$ matrix $H_e(r)$ is defined as

$$H_e(r) = \begin{bmatrix} H(r) \\ \dfrac{\partial H(r)}{\partial r_1} \\ \dfrac{\partial \left(\begin{bmatrix} 0 & 1 \end{bmatrix} H(r) \right)}{\partial r_2} \end{bmatrix} = \begin{bmatrix} H(r) \\ \dfrac{\partial \left(\begin{bmatrix} 1 & 0 \end{bmatrix} H(r) \right)}{\partial r_1} \\ \dfrac{\partial H(r)}{\partial r_2} \end{bmatrix}.$$

The equivalence of the two definitions for $H_e(r)$ can be concluded from

$$\frac{\partial(\begin{bmatrix} 0 & 1 \end{bmatrix} H(r))}{\partial r_1} = \frac{\partial(\begin{bmatrix} 1 & 0 \end{bmatrix} H(r))}{\partial r_2}$$

which is a consequence of Maxwell's equations [17].

For four electromagnets ($n = 4$), the unique solution of the linear equation (18) can be obtained by left multiplying both sides of the equation by the inverse of $F(\phi)H_e(r)$, if this inverse exists. When $n > 4$, the number of unknowns in (18) exceeds the number of equations, thus the solution of this equation is not unique. In order to determine the set of solutions for this case, we employ the singular value decomposition [27]

$$FH_e = U \begin{bmatrix} D & 0_{4\times(n-4)} \end{bmatrix} V^T \tag{19}$$

where D is a diagonal matrix and U and V are 4×4 and $n \times n$ unitary matrices, respectively. Considering (19), it is easy to verify that

$$y = V \begin{bmatrix} z \\ q \end{bmatrix}$$

satisfies (18) for every $q \in \mathbb{R}^{n-4}$, if z is the unique solution of

$$UDz = \rho e + \frac{1}{\rho} Ex.$$

By solving this equation for z, the family of solutions for (15) is obtained as

$$y(r, x; \rho, \phi, q) = \rho b_1(r, \phi) + \frac{1}{\rho} B_2(r, \phi)x + B_3(r, \phi)q \tag{20}$$

where

$$\begin{aligned} b_1 &= V \begin{bmatrix} D^{-1}U^T e \\ 0_{(n-4)\times 1} \end{bmatrix} \\ B_2 &= V \begin{bmatrix} D^{-1}U^T E \\ 0_{(n-4)\times 2} \end{bmatrix} \\ B_3 &= V \begin{bmatrix} 0_{4\times(n-4)} \\ I_{n-4} \end{bmatrix}. \end{aligned} \tag{21}$$

This expression can be modified for $n = 4$ by dropping its last term on the right-hand side, i.e.,

$$y(r, x; \rho, \phi) = \rho b_1(r, \phi) + \frac{1}{\rho} B_2(r, \phi)x. \tag{22}$$

B. Optimal Solution

Among all the solutions of (15) represented by the parametric expression (20), we seek the solution which minimizes the quadratic cost function

$$J = y^T W(r, x) y \tag{23}$$

where $W(r, x)$ is a $n \times n$ positive definite matrix, generally depending on r and x. A typical candidate for $W(r, x)$ is the $n \times n$ identity matrix which leads to the minimum Euclidean norm of y. Since under our assumptions, y is approximately equal to the control vector, this condition can be interpreted as the minimum control effort. Later in this section, we introduce a weight matrix $W(r, x)$ which leads to a robust solution against the uncertainty in the modeling of $g(\cdot)$.

In order to minimize (23), we substitute the parametric solution (20) into this cost function, fix the variables r and x, and minimize J with respect to ρ, ϕ, and q. This minimization can be performed in three steps: minimizing J with respect to q with ρ and ϕ fixed, next minimizing with respect to ρ with ϕ fixed, and finally, minimizing with respect to ϕ.

Since $B_3^T W B_3$ is a positive definite matrix, for every fixed (r, x) and (ρ, ϕ), the cost function J has a unique minimum with respect to q whose associated minimum point is the solution of

$$\frac{\partial J}{\partial q} = 2B_3^T W \left(\rho b_1 + \frac{1}{\rho} B_2 x + B_3 q \right) = 0.$$

We substitute the solution

$$q^* = -\left(B_3^T W B_3\right)^{-1} B_3^T W \left(\rho b_1 + \frac{1}{\rho} B_2 x \right)$$

of this linear equation into (20) to obtained its optimized form

$$y_q^*(r, x; \rho, \phi) = \rho \tilde{b}_1(r, x, \phi) + \frac{1}{\rho} \tilde{B}_2(r, x, \phi)x$$

where

$$\begin{aligned} \tilde{b}_1(r, x, \phi) &= M(r, x, \phi) b_1(r, \phi) \\ \tilde{B}_2(r, x, \phi) &= M(r, x, \phi) B_2(r, \phi) \end{aligned}$$

with the $n \times n$ matrix M defined as

$$M = I_n - B_3 \left(B_3^T W B_3\right)^{-1} B_3^T W.$$

Let J_q^* be the cost function (23) with y replaced with y_q^*. We fix ϕ and minimize J_q^* with respect to ρ. The extremum of J_q^* is attained at the solution of

$$\frac{\partial J_q^*}{\partial \rho} = 2\rho \tilde{b}_1^T W \tilde{b}_1 - \frac{2}{\rho^3} x^T \tilde{B}_2^T W \tilde{B}_2 x = 0 \tag{24}$$

which can be explicitly expressed as

$$\rho^*(r, x, \phi) = \left(\frac{x^T \tilde{B}_2^T(r, x, \phi) W(r, x) \tilde{B}_2(r, x, \phi) x}{\tilde{b}_1^T(r, x, \phi) W(r, x) \tilde{b}_1(r, x, \phi)} \right)^{1/4}.$$

We note that

$$\frac{\partial^2 J_q^*}{\partial \rho^2} = 2\tilde{b}_1^T W \tilde{b}_1 + \frac{6}{\rho^4} x^T \tilde{B}_2^T W \tilde{B}_2 x > 0$$

implying that ρ^* is the minimum point of J_q^*. The optimized form of $y_q^*(r,x;\rho,\phi)$ is now given by

$$y_{\rho,q}^*(r,x;\phi)=\rho^*(r,x,\phi)\tilde{b}_1(r,x,\phi)+\frac{\tilde{B}_2(r,x,\phi)x}{\rho^*(r,x,\phi)}.$$

Finally, we minimize the cost function

$$J_{\rho,q}^*(r,x,\phi)=(y_{\rho,q}^*(r,x;\phi))^T W(r,x) y_{\rho,q}^*(r,x;\phi)$$

with respect to ϕ. Upon solving the optimization problem

$$\phi^*(r,x)=\arg\min_{\phi\in[0,\pi)} J_{\rho,q}^*(r,x,\phi) \tag{25}$$

we get the inverse map

$$g^{-1}(r,x)=y_{\rho,q}^*(r,x;\phi^*(r,x)).$$

This problem is normally solved by means of numerical techniques.

According to our definition, the domain of ϕ is $[0,2\pi)$, while we have limited the search interval of (25) to $[0,\pi)$. We note that $F(\phi)$ has the property that $F(\phi+\pi)=-F(\phi)$. The facts that this property is passed to $y_{\rho,q}^*(r,x;\phi)$ and that $J_{\rho,q}^*(r,x,\phi)$ is quadratic in $y_{\rho,q}^*$ imply that

$$J_{\rho,q}^*(r,x,\phi+\pi)=J_{\rho,q}^*(r,x,\phi)$$

i.e., the function is periodic in ϕ with a period of π. Thus, over the original domain of $[0,2\pi)$, this function has at least two minima which correspond to y and $-y$ (a direct consequence of the force depending on the square of the magnetic field). This type of double minima can be avoided by shrinking the search interval to $[0,\pi)$, and therefore, does not affect the performance of the closed-loop system. However, there is another type of multiple minima with severe consequences on the control performance. This issue is discussed and resolved in Section IV-D.

C. Extension to Three-Dimensional Space

We note that the linear equation (17) is equally valid for both cases of $m=2$ and $m=3$. To extend the results of Sections IV-A and IV-B to the third dimension, $p\in\mathbb{R}^3$ is represented in a spherical coordinate system according to

$$p=\rho[\cos\phi_1\cos\phi_2 \quad \cos\phi_1\sin\phi_2 \quad \sin\phi_1]^T$$

where $\rho\geqslant 0$, $\phi_1\in[0,2\pi)$, and $\phi_2\in[0,\pi)$. With this representation of p, the linear equation (17) can be written as (18), albeit with new definitions for the matrices $F(\phi)$, $H_e(r)$, E, and e. We redefine $e=[1 \quad 0_{1\times 5}]^T$, $E=[0_{3\times 3} \quad \frac{1}{2}I_3]^T$, and

$$H_e(r)=\begin{bmatrix} H(r) \\ \dfrac{\partial H(r)}{\partial r_1} \\ \dfrac{\partial([0_{2\times 1} \quad I_2]H(r))}{\partial r_2} \\ \dfrac{\partial([0 \quad 0 \quad 1]H(r))}{\partial r_3} \end{bmatrix}.$$

In this case, $F(\phi)$ is a function of the two-dimensional vector $\phi=(\phi_1,\phi_2)$ and is defined as

$$F(\phi)=\begin{bmatrix} F_{11}(\phi) & 0_{3\times 3} & 0_{3\times 3} \\ 0_{3\times 3} & F_{22}(\phi) & F_{23}(\phi) \end{bmatrix}$$

where

$$F_{11}(\phi)=\begin{bmatrix} \cos\phi_1\cos\phi_2 & \cos\phi_1\sin\phi_2 & \sin\phi_1 \\ -\sin\phi_2 & \cos\phi_2 & 0 \\ -\sin\phi_1\cos\phi_2 & -\sin\phi_1\sin\phi_2 & \cos\phi_1 \end{bmatrix}$$

$$F_{22}(\phi)=\begin{bmatrix} \cos\phi_1\cos\phi_2 & \cos\phi_1\sin\phi_2 & \sin\phi_1 \\ 0 & \cos\phi_1\cos\phi_2 & 0 \\ 0 & 0 & \cos\phi_1\cos\phi_2 \end{bmatrix}$$

$$F_{23}(\phi)=\begin{bmatrix} 0 & 0 & 0 \\ \cos\phi_1\sin\phi_2 & \sin\phi_1 & 0 \\ 0 & \cos\phi_1\sin\phi_2 & \sin\phi_1 \end{bmatrix}.$$

The parametric family of solutions for the case of $m=3$ has a form similar to the case of $m=2$, since they both are the solutions of the linear equation (18). Redefining the matrices $b_1(r,\phi)$, $B_2(r,\phi)$, and $B_3(r,\phi)$ similar to (21) but with appropriate dimensions, the parametric family of solutions is given by (22) for $n=6$ and by (20) for $n>6$. For $m=3$, the solution to the optimization problem follows the same procedure of Section IV-B, except for a minor modification in the last step (25), in which minimization must be performed with respect to the two-dimensional vector ϕ over the search region $\phi\in[0,\pi)\times[0,\pi)$.

D. Spatial Discontinuity of the Optimal Solution

Numerical studies with $m=2$ indicate that there exists a subset of $\mathscr{C}$ denoted by $\mathscr{C}'$ such that for every $r\in\mathscr{C}'$ the cost function $J_{\rho,q}^*(r,x,\phi)$ has one global and one local minimum on the interval $\phi\in[0,\pi)$. Also, at some points r in $\mathscr{C}'$, the global and the local minima are equal, i.e., $J_{\rho,q}^*(r,x,\phi)$ has two global minima. The set of these points represents a curve in $\mathscr{C}'$ which will be denoted by $\mathcal{C}$. The important property of this curve is that the optimal solution $\phi^*(r,x)$ is discontinuous at every $r\in\mathcal{C}$. The origin of this discontinuity is depicted in Fig. 5. According to this figure, when the magnetic particle moves along a trajectory that crosses $\mathcal{C}$, at the point of intersection, the local and the global minima exchange their roles, which leads to a jump in $\phi^*(r,x)$. The inverse map $g^{-1}(r,x)$ inherits the discontinuity of $\phi^*(r,x)$. Fig. 6 illustrates the discontinuity map. For four different desired directions of the vector x (the magnetic force is proportional to x), the figure shows the magnetic particle spatial locations across which the inverse map jumps.

As the magnetic particle is controlled along its trajectory, the spatial discontinuity of the inverse map gives rise to a temporal discontinuity of $\tilde{y}(t)$, which in turn creates a spiky error in the trajectory of the particle while crossing the discontinuity curve $\mathcal{C}$. This type of error might be negligible if the bandwidth σ_s of the electromagnets (or its equivalent σ_s^* after compensation) is large enough, in particular for those applications in which crossing the discontinuity curve is infrequent. However, when

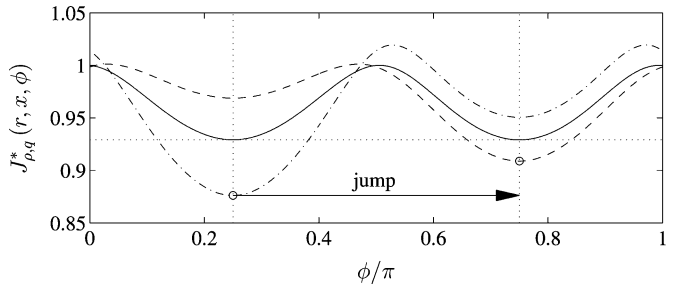

Fig. 5. Origin of the discontinuity of $\phi^*(r,x)$ for the case of $m = 2$. The graphs are calculated for four $(n = 4)$ typical electromagnets and the weight matrix $W(r,x) = I_4$. The solid curve is associated with a point at $r \in \mathcal{C}$ and the two other curves represent two particle positions on each side of the $\mathcal{C}$ dividing boundary. The jump in the optimal solution is marked by the two circles.

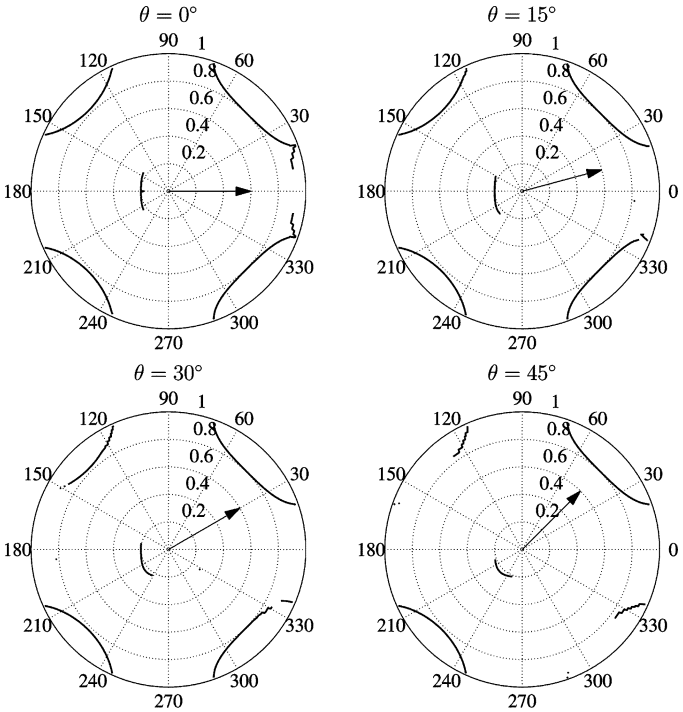

Fig. 6. Discontinuity map for a desired magnetic force in the direction of $x = [\cos\theta \ \sin\theta]^T$ with $\theta = 0°, 15°, 30°$, and $45°$. The figure shows the particle locations across which the inverse map $g^{-1}(r,x)$ is discontinuous. Here it is assumed that $\mathscr{C}$ is a unit circle $(m = 2)$ and $n = 4$ identical electromagnets are placed at the angles 0°, 90°, 180°, and 270°. The behavior for desired magnetic force directions in the remaining seven octants can be inferred from symmetry and is not shown.

a specific application requires frequent crossing of the discontinuity curve and the bandwidth σ_s is not large enough for sufficiently faithful transmission of a discontinuous signal, the resulting error must be compensated by removing the discontinuity of $\tilde{y}(t)$. Clearly, smoothing $\tilde{y}(t)$ by means of a conventional linear low-pass filter is not helpful as it destroys the property of satisfying $g(r,\tilde{y}) = \tilde{x}$. Instead, we develop a class of nonlinear filters which can smooth $\tilde{y}(t)$, while preserving this property.

In order to remove the discontinuity of $\tilde{y}(t)$, we modify the nonlinear controller of Fig. 2 as depicted in Fig. 7 (similar modification can be applied to Fig. 4). According to this figure,

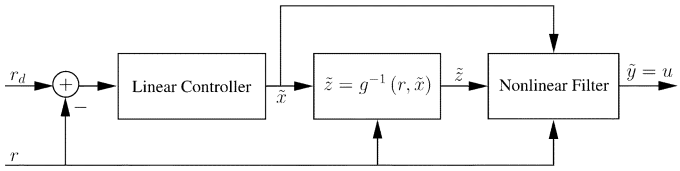

Fig. 7. Block diagram of the controller equipped with a nonlinear filter for removing the discontinuity of $\tilde{y}(t)$.

the first two stages of the modified controller are similar to Fig. 2; however, after generating the discontinuous signal $\tilde{z}(t) = g^{-1}(r(t),\tilde{x}(t))$, it is passed through a nonlinear filter to obtain the smooth control $u(t) = \tilde{y}(t)$. The output $\tilde{y}(t)$ of this controller, while being a smooth version of $\tilde{z}(t)$, satisfies the constraint $g(r,\tilde{y}) = \tilde{x}$. Note that $g(r,\tilde{y}) = \tilde{x}$ constrains m degrees of freedom out of n, thus $n - m$ remaining degrees of freedom are incorporated by the filter to generate a smooth output. When a parameter σ_c of this filter, which is the counterpart of bandwidth in linear filters, is properly tuned, the output $\tilde{y}(t)$ remains close to the input $\tilde{z}(t)$, except for a short period of time after each discontinuity happens. Therefore, while $\tilde{y}(t)$ is a smooth function of time, it approximately preserves the optimality of $\tilde{z}(t)$.

To establish the relationship between the input $\tilde{z}(t)$ and the output $\tilde{y}(t)$ of the nonlinear filter in Fig. 7, we begin with a linear low-pass filter and modify it to a nonlinear filter whose output $\tilde{y}(t)$ satisfies $g(r,\tilde{y}) = \tilde{x}$, a constraint not satisfied by the original linear filter. We first consider a discrete-time representation of the filter. Assume that the signals $\tilde{z}(t)$, $\tilde{y}(t)$, $\tilde{x}(t)$, and $r(t)$ are sampled uniformly at integer multiples of a sampling period δ and for $k = 0, 1, 2, \ldots$ define $\tilde{z}_k = \tilde{z}(k\delta)$, $\tilde{y}_k = \tilde{y}(k\delta)$, $\tilde{x}_k = \tilde{x}(k\delta)$, and $r_k = r(k\delta)$. Let $\tilde{y}_0 = \tilde{z}_0$ and consider the linear low-pass filter

$$\tilde{y}_k = (1-\lambda)\tilde{y}_{k-1} + \lambda\tilde{z}_k$$

where $0 < \lambda < 1$ is a parameter for adjusting its bandwidth. This linear filter is able to smooth the input signal $\tilde{z}_k$; however, its output does not satisfy the constraint $g(r_k,\tilde{y}_k) = \tilde{x}_k$. To develop a nonlinear version of the filter which satisfies this constraint, instead of updating $\tilde{y}_k$ with $(1-\lambda)\tilde{y}_{k-1}+\lambda\tilde{z}_k$, we update it with the closest vector ξ^* to this linear combination which also satisfies $g(r_k,\xi^*) = \tilde{x}_k$. Thus, the nonlinear filter can be characterized through the optimization problem

$$\tilde{y}_k = \arg\min_{\xi\in\mathbb{R}^n} \|(1-\lambda)\tilde{y}_{k-1} + \lambda\tilde{z}_k - \xi\|$$

subject to $g(r_k,\xi) = \tilde{x}_k$.

Using a more compact notation, this nonlinear filter can be expressed by the recursive equation

$$\tilde{y}_k = \psi((1-\lambda)\tilde{y}_{k-1} + \lambda\tilde{z}_k, r_k, \tilde{x}_k) \tag{26}$$

with the initial state $\tilde{y}_0 = \tilde{z}_0$. In this equation, the mapping $\psi(\cdot) : \mathbb{R}^n \times \mathbb{R}^m \times \mathbb{R}^m \to \mathbb{R}^n$ is defined via the optimization problem

$$\psi(w,r,x) = \arg\min_{\xi\in\mathcal{G}(r,x)} \|\xi - w\| \tag{27}$$

where $\mathcal{G}(r,x)$ is a subset of $\mathbb{R}^n$ defined for every fixed r and x as

$$\mathcal{G}(r,x) = \{y \in \mathbb{R}^n \mid g(r,y) = x\}. \tag{28}$$

In order to compute the nonlinear map $\psi(\cdot)$, the parametric solution (20) is employed to convert the constrained optimization problem (27) to the unconstrained problem

$$(\rho^*, \phi^*, q^*) = \arg\min_{\rho,\phi,q} \|y(r,x;\rho,\phi,q) - w\|. \tag{29}$$

The solution to this optimization problem, which is presented in Appendix A, parallels the three-step procedure followed in the previous subsection to determine $g^{-1}(\cdot)$. After solving the problem, the nonlinear map $\psi(\cdot)$ can be obtained from

$$\psi(w,r,x) = y(r,x;\rho^*(w,r,x),\phi^*(w,r,x),q^*(w,r,x)).$$

The only remaining concern is to settle an argument against the developed filter: considering the similarities between the optimization problem (29) and the one leading to $g^{-1}(\cdot)$, it is expected that $\psi(w,r,x)$ has some discontinuous points with respect to r, as observed in $g^{-1}(r,x)$. In fact, the existence of the discontinuous points depends on the distance of w from the manifold (28), i.e., for a w close to the manifold, $\psi(w,r,x)$ is continuous in r, while the discontinuous points appear when w is far from the manifold (e.g., $w = 0$). The reason behind this statement is that for a w close to the manifold, the global minimum of (29), which is the minimum distance between w and the manifold, is much smaller than any local minimum such that the role of the global and the local minima cannot be exchanged as can happen for a w far from the manifold (see Fig. 5). Since the parameter λ of the filter is typically small, the linear combination $(1-\lambda)\tilde{y}_{k-1} + \lambda\tilde{z}_k$ which substitutes the argument w of $\psi(w,r,x)$ in (26), remains close to the manifold $\mathcal{G}(r_k,\tilde{x}_k)$. This property prevents the filter output from discontinuity.

The continuity of the filter output is assured for the continuous-time version of the filter, since it is obtained as the limiting case of $\lambda \to 0$ and $\delta \to 0$, while keeping λ/δ at a constant value $\sigma_c > 0$. This filter is characterized by the state-space equation[2]

$$\dot{\tilde{y}} = \sigma_c \Psi_w(\tilde{y},r,\tilde{x})(\tilde{z}-\tilde{y}) + \Psi_r(\tilde{y},r,\tilde{x})\dot{r} + \Psi_x(\tilde{y},r,\tilde{x})\dot{\tilde{x}} \tag{30}$$

where the matrices $\Psi_w(\cdot)$, $\Psi_r(\cdot)$, and $\Psi_x(\cdot)$ are defined as

$$\begin{aligned}\Psi_w(w,r,x) &= \frac{\partial\psi(w,r,x)}{\partial w}\\ \Psi_r(w,r,x) &= \frac{\partial\psi(w,r,x)}{\partial r}\\ \Psi_x(w,r,x) &= \frac{\partial\psi(w,r,x)}{\partial x}.\end{aligned} \tag{31}$$

In Appendix B, this equation is derived from the discrete-time filter (26). The parameter σ_c of the filter is the analogue of bandwidth for linear filters and is directly connected to the physical parameters of the system. In particular, it must be chosen to satisfy $\sigma_c \ll \sigma_s$ (σ_s is the electromagnet bandwidth) in order to ensure distortionless transmission of the filter output through the electromagnets.

[2]For the sake of simplicity, the time dependence of the vectors $\bar{y}(t)$, $\bar{z}(t)$, $r(t)$, and $\bar{x}(t)$ is not explicitly shown.

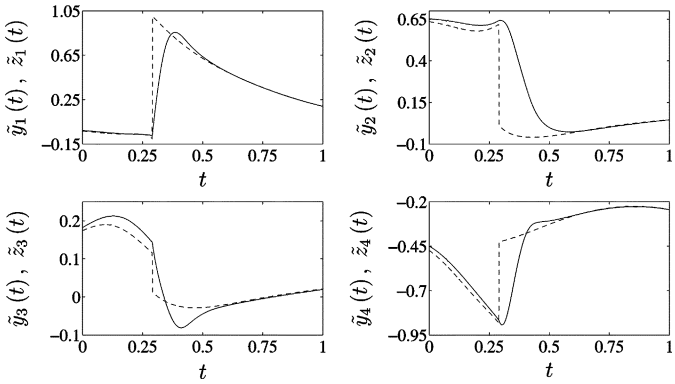

Fig. 8. Input $\bar{z}(t)$ (dashed line) and output $\bar{y}(t)$ (solid line) of the nonlinear filter (30) for removing the spatial discontinuity of the inverse map with an arrangement of $n = 4$ identical electromagnets. It is assumed that $\mathscr{C}$ is a unit circle ($m = 2$) and the electromagnets 1 through 4 are placed at 0°, 90°, 180°, and 270°, respectively. The position vector $r(t)$ changes with a unit velocity along a straight line from $(-0.5\cos 20°, 0.5\sin 20°)$ to $(0.5\cos 20°, -0.5\sin 20°)$. The vertical axes are normalized to $u_{\max}$.

To evaluate the performance of the nonlinear filter (30) and to demonstrate its ability to remove the discontinuity of $\tilde{z}(t) = g^{-1}(r(t),\tilde{x}(t))$, we have run a series of computer simulations. Some results of this study are presented in Fig. 8. In this figure, the input $\tilde{z}(t)$ and the output $\tilde{y}(t)$ of the nonlinear filter (30) are illustrated versus time to show how the filter can suppress the discontinuity of its input at $t = 0.3$. The filter parameters are $n = 4$ and $\sigma_c = 20$ and the output is obtained from the discrete-time filter (26), albeit with a small enough sampling period to ensure that the discrete-time output is a close approximation of $\tilde{y}(t)$. It is assumed that $\mathscr{C}$ is a unit circle ($m = 2$) and the electromagnets 1 through 4 are placed at 0°, 90°, 180°, and 270°, respectively. The particle position vector $r(t)$ moves with a unit velocity along a straight line from $(-0.5\cos 20°, 0.5\sin 20°)$ to $(0.5\cos 20°, -0.5\sin 20°)$, while $\tilde{x}(t)$, the desired direction of motion, is the constant vector $(\cos 20°, -\sin 20°)$.

E. Robust Solution

Suppose that there is an error of $\delta h(r,y)$ in modeling of the magnetic field, i.e., we model the magnetic field by $H(r)y$, while the actual magnetic field is $H(r)y + \delta h(r,y)$. Accordingly, we express $g(\cdot)$ by (8) while its actual value is given by

$$g_a(r,y) = \nabla\|H(r)y + \delta h(r,y)\|^2. \tag{32}$$

Certainly, the inverse map $g^{-1}(\cdot)$ which is derived from $g(\cdot)$ is not the exact inverse of $g_a(\cdot)$; however, the parameters of (20) can be obtained to minimize the induced error

$$J_a = \|g_a(r, g^{-1}(r,x)) - x\|. \tag{33}$$

In order to obtain the robust inverse map $g^{-1}(\cdot)$ which minimizes (33), we first expand the right-hand side of (32) and ignore the second-order error $\|\delta h(r,y)\|^2$ to get

$$\begin{aligned} g_a(r,y) &\simeq \nabla\|H(r)y\|^2 + 2\nabla(\delta h^T(r,y)H(r)y)\\ &= g(r,y) + 2\delta H_a^T(r,y)H_e(r)y\end{aligned}$$

where the 2×5 matrix $\delta H_a^T(r,y)$ is defined as

$$\delta H_a^T(r,y) = \begin{bmatrix} \dfrac{\partial \delta h^T(r,y)}{\partial r_1} & \delta h^T(r,y) & 0 \\ \dfrac{\partial \delta h^T(r,y)}{\partial r_2} & 0 & \delta h^T(r,y) \end{bmatrix}.$$

Using this result, (33) can be expressed as

$$J_a = 2 \left\| \delta H_a^T(r,y) H_e(r) y \right\|.$$

Since $\delta H_a^T(r,y)$ is not known, it is not possible to exactly minimize J_a; however, we can minimize an upper bound of J_a. In determining this upper bound, different methods can be used [28], [29]; our approach is to explore the properties of matrix norms [27] to get

$$J_a \leqslant 2 \|\delta H_a(r,y)\| \cdot \|H_e(r) y\|$$

where $\|\delta H_a(r,y)\|$ denotes the induced Euclidean norm of $\delta H_a(r,y)$. In order to minimize this upper bound, we need to minimize $\|H_e(r)y\|$, which is equivalent to minimizing

$$J = y^T \left(H_e^T(r) H_e(r) \right) y. \tag{34}$$

Thus, the weight matrix associated with the robust inverse map is given by

$$W(r) = H_e^T(r) H_e(r). \tag{35}$$

We note that the rank of this matrix is not larger than the rank of $H_e(r)$ which is at most $m_e = m(m+3)/2$. Thus, for $n > m_e$, the problem of minimizing (34) subject to the constraint (18) does not have a unique solution. To show this fact, we substitute $p_e = H_e(r)y$ into our optimization problem to reformulate it as minimizing

$$J = p_e^T p_e$$

subject to

$$F(\phi) p_e = \rho e + \frac{1}{\rho} E x.$$

The unique solution $p_e^*(x)$ of this problem can be obtained using the procedure of Section IV-B. Next, we solve the linear equation $H_e(r)y = p_e^*(x)$ to obtain the optimal value of y. Since this equation is underdetermined, it has a family of solutions instead of a unique one. Among all solutions in this family, it is desirable to choose the one with the minimum Euclidean norm. Using the Moore-Penrose pseudoinverse [27] of $H_e(r)$, this solution is given by

$$y^*(r,x) = H_e^T(r) \left(H_e(r) H_e^T(r) \right)^{-1} p_e^*(x). \tag{36}$$

This result can be also obtained as the unique solution of the original optimization problem by replacing (35) with the full rank matrix

$$W(r) = H_e^T(r) H_e(r) + H_e^{\perp}(r) (H_e^{\perp}(r))^T \tag{37}$$

where $H_e^{\perp}(r)$ is any $n \times (n - m_e)$ matrix satisfying

$$H_e(r) H_e^{\perp}(r) = 0_{m_e \times (n-m_e)}.$$

The robust solution (36) is a continuous function of the position vector r, in opposite to the minimum effort solution. Although both robustness and continuity of this solution are of great advantage, a pure robust solution is difficult to use in practice due to its required large control effort $\|y\|$. Control effort can be significantly reduced, while effectively preserving robustness, by introducing an identity regularization matrix [30] to modify (35) as

$$W(r) = \epsilon I_n + \frac{H_e^T(r) H_e(r)}{\|H_e^T(r) H_e(r)\|} \tag{38}$$

where ϵ is a small positive scalar and I_n is the $n \times n$ identity matrix. Clearly, this modification represents a tradeoff between robustness and control effort.

For every control vector $y \in \mathbb{R}^n$ which satisfies $g(r,y) = x$, the nonnegative quantity $\|H_e(r)y\|$ is a measure for the sensitivity of control to modeling errors. To make this quantity more meaningful, we normalize it with respect to $\|H_e(r) y_{\text{rob}}\|$, where the robust solution y_{rob} solves the optimization problem with the weight matrix (37). Hence, for every r and x we define the relative sensitivity of control as

$$\eta(r,x) = \frac{\|H_e(r)y\|}{\|H_e(r) y_{\text{rob}}\|}.$$

Considering that $\|H_e(r)y\|$ attains its minimum at $y = y_{\text{rob}}$, the relative sensitivity metric $\eta(r,x)$ is not smaller than 1 and a larger $\eta(r,x)$ corresponds to a more sensitive control (values of $\eta(r,x)$ closer to 1 are associated with a more robust control). We are particularly interested in the relative sensitivity of the minimum effort control, i.e., the case where y minimizes $J = \|y\|$ subject to $g(r,y) = x$. For this case, Fig. 9 illustrates the contour maps of $\eta(r,x)$ with respect to the particle position r for different directions of x (directions of the desired magnetic force). A comparison between this figure and Fig. 6 indicates a close relationship between the robustness and the spatial discontinuity discussed in Section IV-D, in the sense that the control is most sensitive to the modeling errors in the vicinity of the discontinuity curves $\mathcal{C}$.

V. Simulation and Experimental Results

We analyze the performance of our control algorithm via simulations and an experiment. In the simulations, we assume that $\mathscr{C}$ is a circle with radius a and $n = 4$ identical electromagnets are equally spaced around this circle. This configuration is in accordance with the design of our experimental testbed which is shown in Fig. 10. Our setup includes four solenoids, a petri dish containing a ferrofluid droplet in a viscous surrounding fluid (oil), and a camera on the top which combined with an image processing software measures the position of the droplet. Fig. 10(b) shows a measured trajectory for a 2.5 μL ferrofluid droplet being controlled around a spiral trajectory at a velocity of 0.1 cm/s. For details on the experimental setup and materials see [16].

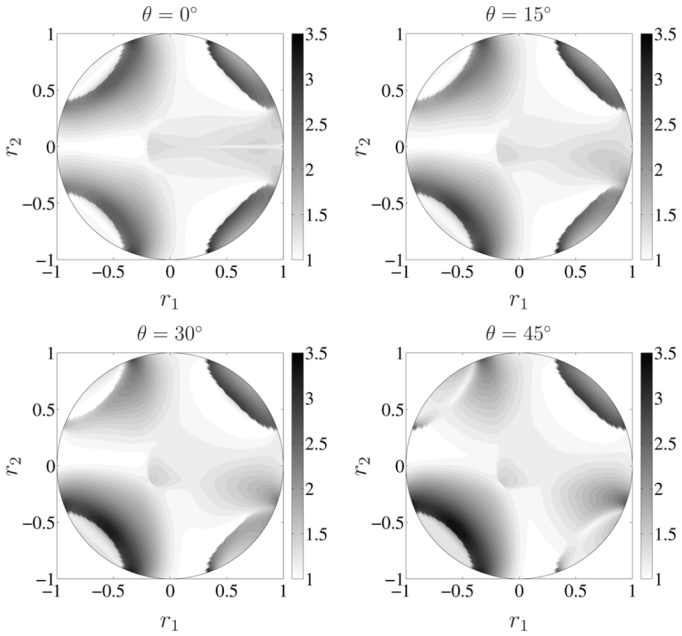

Fig. 9. Contour maps of the relative sensitivity metric $\eta(r, x)$ (with respect to the position vector r) for the minimum effort control and corresponding to a desired magnetic force in the direction of $x = [\cos\theta \quad \sin\theta]^T$ with $\theta = 0°, 15°, 30°$, and 45°. Again it is assumed that $\mathscr{C}$ is a unit circle ($m = 2$) and $n = 4$ identical electromagnets are placed at the angles 0°, 90°, 180°, and 270°. Dark coloring shows locations of high sensitivity.

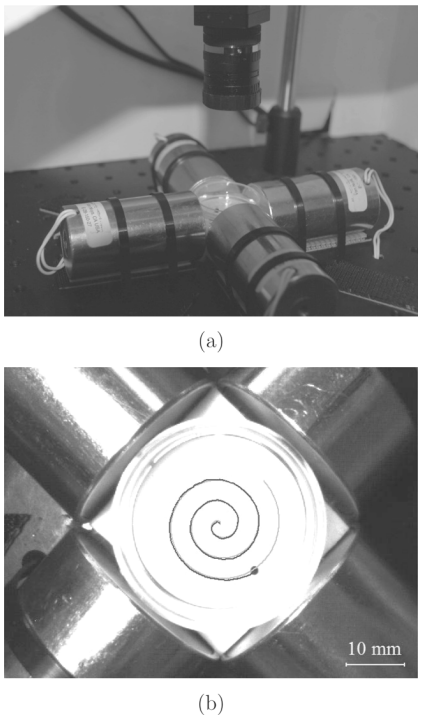

(a)

(b)

Fig. 10. Experimental testbed: (a) the main components of the system including four solenoids, a petri dish containing a ferrofluid droplet in a viscous surrounding fluid, and a camera on the top; (b) the trajectory of the ferrofluid (leading droplet and black path) recorded by the camera during an experiment to steer the droplet along a desired spiral trajectory (gray underlying path).

In the simulations, we used the state-space model (11) with $d(t) = 0$ and model parameters which were matched to the experimental testbed. All parameters were directly measured or

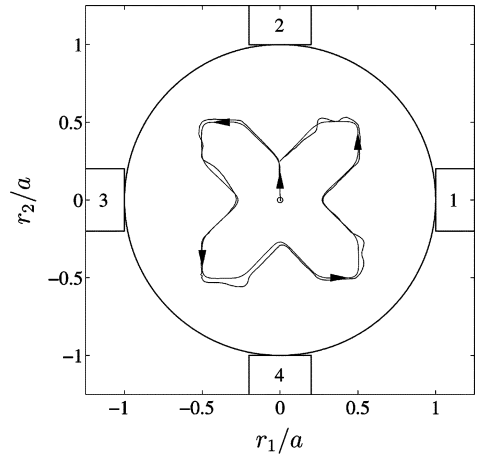

Fig. 11. Magnetic particle tracks an x-shaped trajectory. The black and gray lines represent the experimental and simulated actual trajectories, respectively. In this figure, the desired trajectory is not shown since its deviation from the simulated actual trajectory is not visible. The small rectangles marked with 1 through 4 represent the electromagnets.

were extracted from empirical data using system identification techniques. The implemented controller has the nonlinear structure of Fig. 7 while its linear block is a proportional controller with a gain $k_p > 0$, i.e.,

$$\tilde{x}(t) = k_p(r_d(t) - r(t)).$$

With this choice for the linear controller, the closed-loop system of Fig. 3 represents second order linear dynamics in each channel of r_1 and r_2 with a transfer function

$$G_c(s) = \frac{\omega_n^2}{s^2 + 2\zeta\omega_n s + \omega_n^2}.$$

The parameters of this model are estimated to be $\zeta = 0.77$ and $\omega_n = 1.87$ rad/s.

The time constant $1/\sigma_s$ of the electromagnets is obtained as $\sigma_s = 59\omega_n$ by direct measurement. Since the electromagnets are identical and their mutual inductance is negligible, we let $A = \Omega = I_4$. We note that the bandwidth of the closed-loop system is roughly $BW = \omega_n$, thus the condition $\sigma_s = 59BW \gg BW$ is well satisfied. The system parameter σ_v is identified to be $\sigma_v = 1.54\omega_n$ and k_p is chosen such that $k_p k_g = 0.12$. Also, the parameter of the nonlinear filter (30) is set to $\sigma_c = 5.7\omega_n$. The controller is implemented digitally on a personal computer with a sampling rate $7.7\omega_n$.

The magnetic fields $h_k(r)$ are determined from (2) in terms of the magnetic field $h_c(r)$ of a single magnet. An analytical expression for $h_c(r)$ is presented in Appendix C which is incorporated with parameters $\varrho = 0.4a$ and $l = 4a$ for both simulations and controller implementation. This expression provides an exact description of the magnetic field due to an air core solenoid (for simplicity), while we use iron core solenoids in our experiment. As a consequence, our calculation of the magnetic field is not precise in particular at points very close to the face of the solenoids. To minimize the effect of this error, we incorporate the robust solution of Section IV-E for the points close to the face of the solenoids while using the minimum control effort

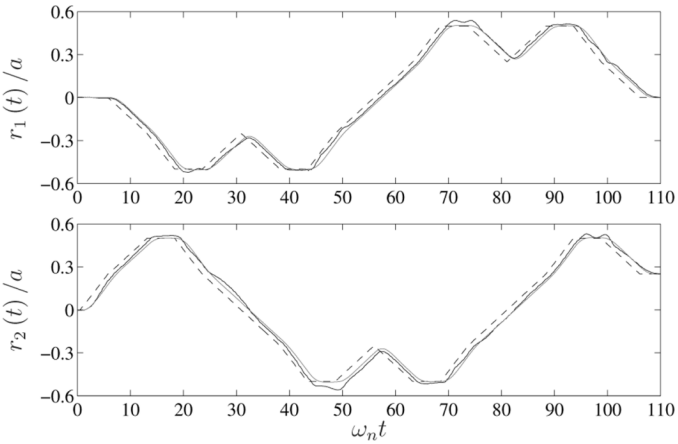

Fig. 12. Desired position (dashed line) and actual position of the magnetic particle versus time, obtained experimentally (black solid line) and by simulation (gray solid line).

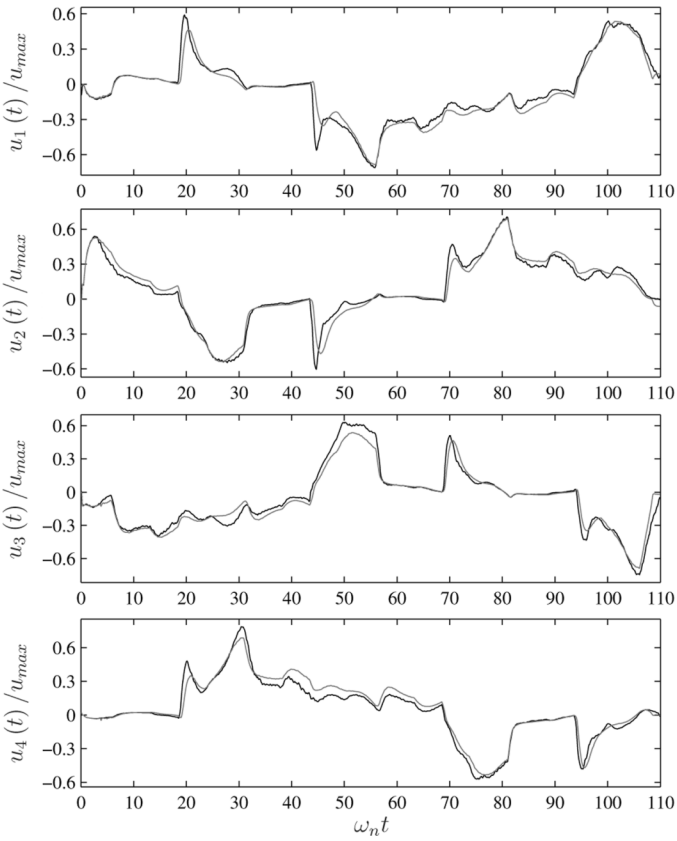

Fig. 13. Control vector $u(t)$ versus time, obtained from experiment (black line) and by simulation (gray line).

solution near the center of the circular region $\mathscr{C}$. For this purpose, we have designed a weight matrix $W(r)$ which smoothly shifts from (38) with $\epsilon = 0.01$ at $\|r\| = a$ into the identity matrix at $\|r\| = 0$.

We present the results of simulations and experiment in parallel so that they can be easily compared. For the sake of simplicity, these results are illustrated in a normalized scale such that time, voltage, and length are normalized to $\tau_{cl} = 1/\omega_n$,

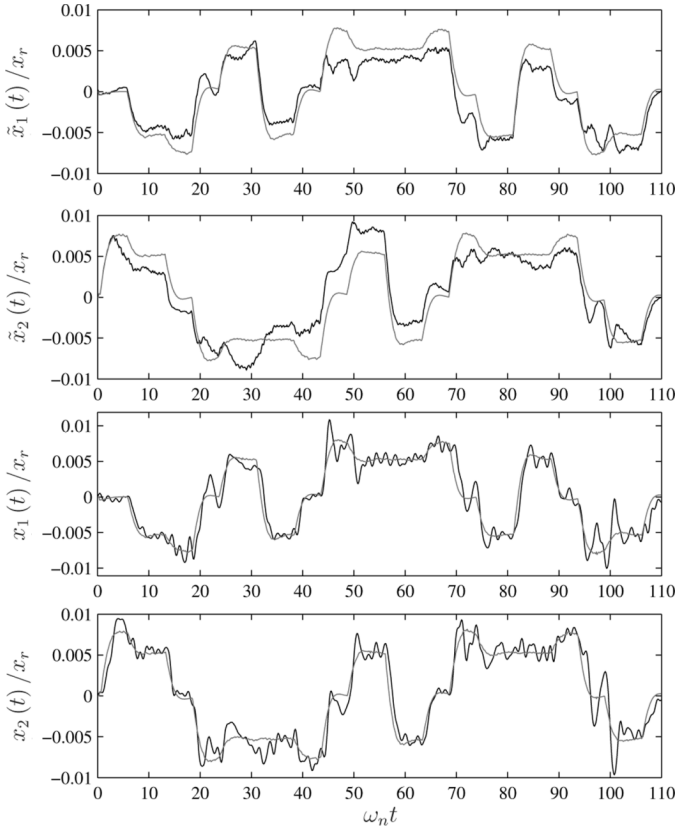

Fig. 14. Experimental (black line) and simulated (gray line) graphs of $\tilde{x}(t)$ (proportional to the desired magnetic force) and $x(t)$ (proportional to the actual magnetic force) versus time.

$u_{\max} = 20$ V, and $a = 1.75$ cm, respectively. In addition, $x(t)$ and $\tilde{x}(t)$ will be normalized to the quantity

$$x_r = \frac{1}{a}\left(\frac{u_{\max}\|h_c(0)\|}{R^*}\right)^2.$$

We choose an x-shaped desired trajectory for both experiment and simulations, as depicted in Fig. 11. The desired position $r_d(t)$ moves along this trajectory with an average velocity of $0.046a\omega_n$ equivalent to 0.15 cm/s. We intentionally choose a large value for this velocity to make the deviation of the actual trajectory from the desired trajectory visible. According to Fig. 11, the magnetic particle, which is initially located at the origin, moves towards the x-shaped trajectory and closely tracks it. The desired position and the actual position of the magnetic particle obtained from the experiment and by simulation are illustrated as a function of time in Fig. 12. For this trajectory, the control vector $u(t)$ and the pair of $\tilde{x}(t)$ and $x(t)$ are illustrated versus time in Figs. 13 and 14, respectively.

VI. Conclusion

The problem of steering a magnetic particle by controlling a magnetic field has been considered and a class of closed-loop control laws has been developed to optimally shape the magnetic field in time and space in order to drive the particle along any desired trajectory. The magnetic particle moves inside a liquid under the influence of fluid resistance and a magnetic

force generated by an arrangement of electromagnets with adjustable voltages. The dynamics of this system has been described by a cascade combination of three building blocks: a linear low-pass model describing the voltage-current relationship of the electromagnets, a memoryless nonlinear map representing the magnetic force in terms of the electrical currents, and another linear dynamical model describing the motion of the particle under the magnetic force and fluid resistance.

The proposed control law compensates the nonlinear memoryless block by an inverse nonlinear map which is a building block of the controller. Considering that the inverse map is not unique, the best inverse map has been determined by formulating and solving a constrained optimization problem. While this optimization problem can address a wide range of optimality criteria, two important cases of minimum control effort and maximum robustness against modeling errors have been considered. In addition, a disadvantage of the optimal inverse map, a spatial discontinuity, has been discussed and a nonlinear filtering scheme has been developed to remove it. The high performance of the control law in driving the magnetic particle along arbitrary trajectories has been verified both in simulations and in an experiment.

Appendix A
Solution of the Optimization Problem (29)

Our goal is to minimize the cost function

$$J = \left\| \rho b_1(r,\phi) + \frac{1}{\rho} B_2(r,\phi)x + B_3(r,\phi)q - w \right\|^2 \qquad (39)$$

with respect to q, ρ, and ϕ. Similar to Section IV-B, we perform this task in three steps: minimizing J with respect to q while (ρ,ϕ) is fixed, next minimizing with respect to ρ while ϕ is fixed, and finally, minimizing with respect to ϕ.

For a fixed (ρ,ϕ), we obtain the minimum of J with respect to q by setting

$$\frac{\partial J}{\partial q} = 2B_3^T \left(\rho b_1 + \frac{1}{\rho} B_2 x + B_3 q - w \right) = 0.$$

Solving this linear equation for q, we obtain the optimal value

$$q^* = \left(B_3^T B_3\right)^{-1} B_3^T w$$

noting that $B_3^T b_1 = 0$ and $B_3^T B_2 = 0$. Upon substituting this result into the cost function (39), we determine its value J_q^* minimized with respect to q as

$$J_q^* = \left\| \rho b_1(r,\phi) + \frac{1}{\rho} B_2(r,\phi)x - M_I(r,\phi)w \right\|^2$$

where

$$M_I = I_n - B_3(B_3^T B_3)^{-1} B_3^T.$$

We simplify this cost function as

$$J_q^* = b_1^T b_1 \rho^2 - 2b_1^T w\rho - 2x^T B_2^T w\rho^{-1} + x^T B_2^T B_2 x \rho^{-2} + 2b_1^T B_2 x + w^T M_I w. \qquad (40)$$

Since the coefficients $b_1^T b_1$ and $x^T B_2^T B_2 x$ are positive, this function has a global minimum which can be obtained from the roots of its derivative. This means that the global minimizer is one of the roots of the polynomial equation

$$b_1^T b_1 \rho^4 - b_1^T w\rho^3 + x^T B_2^T w\rho - x^T B_2^T B_2 x = 0.$$

By solving this equation, we obtain the global minimizer ρ^*.

Upon substituting ρ^* into (40), we get $J_{q,\rho}^*(r,x,w,\phi)$ which is the minimum cost with respect to (q,ρ). In the last step, we minimize this cost function with respect to ϕ, i.e.,

$$\phi^*(r,x,w) = \arg \min_{\phi \in \mathscr{S}} J_{q,\rho}^*(r,x,w,\phi)$$

where $\mathscr{S} = [0,\pi)$ for $m = 2$ or $\mathscr{S} = [0,\pi) \times [0,\pi)$ if $m = 3$.

Appendix B
Derivation of the Continuous-Time Filter

In order to obtain the continuous-time filter (30), we substitute $\lambda = \sigma_c \delta$ into (26) and rewrite the equation as

$$\tilde{y}_k = \psi(\tilde{y}_{k-1} + \sigma_c\delta(-\tilde{y}_{k-1} + \tilde{z}_k), r_{k-1} + \delta r_k, \tilde{x}_{k-1} + \delta\tilde{x}_k)$$

where $\delta r_k = r_k - r_{k-1}$ and $\delta\tilde{x}_k = \tilde{x}_k - \tilde{x}_{k-1}$. Assuming that the partial derivatives of $\psi(w,r,x)$ with respect to w, r, and x exist, we expand the right-hand side of this equation into a Taylor series around $(\tilde{y}_{k-1}, r_{k-1}, \tilde{x}_{k-1})$ up to first order to approximate

$$\begin{aligned}\tilde{y}_k \simeq\ & \psi(\tilde{y}_{k-1}, r_{k-1}, \tilde{x}_{k-1}) \\ & + \Psi_w(\tilde{y}_{k-1}, r_{k-1}, \tilde{x}_{k-1})\sigma_c\delta(-\tilde{y}_{k-1} + \tilde{z}_k) \\ & + \Psi_r(\tilde{y}_{k-1}, r_{k-1}, \tilde{x}_{k-1})\delta r_k \\ & + \Psi_x(\tilde{y}_{k-1}, r_{k-1}, \tilde{x}_{k-1})\delta\tilde{x}_k \end{aligned} \qquad (41)$$

where the matrices $\Psi_w(\cdot)$, $\Psi_r(\cdot)$, and $\Psi_x(\cdot)$ are defined in (31). From the definition of $\psi(\cdot)$, it is easy to show that

$$\psi(\tilde{y}_{k-1}, r_{k-1}, \tilde{x}_{k-1}) = \tilde{y}_{k-1}$$

which can be used to rewrite (41) as

$$\begin{aligned}\frac{\tilde{y}_k - \tilde{y}_{k-1}}{\delta} =\ & \sigma_c \Psi_w(\tilde{y}_{k-1}, r_{k-1}, \tilde{x}_{k-1})(\tilde{z}_k - \tilde{y}_{k-1}) \\ & + \Psi_r(\tilde{y}_{k-1}, r_{k-1}, \tilde{x}_{k-1})(\delta r_k/\delta) \\ & + \Psi_x(\tilde{y}_{k-1}, r_{k-1}, \tilde{x}_{k-1})(\delta\tilde{x}_k/\delta).\end{aligned}$$

Substituting $\tilde{y}_k = \tilde{y}(k\delta)$, $\tilde{z}_k = \tilde{z}(k\delta)$, $r_k = r(k\delta)$, and $\tilde{x}_k = \tilde{x}(k\delta)$ into this equation and taking limit at $\delta \to 0$, we get (30).

APPENDIX C
COMPUTATION OF THE MAGNETIC FIELD

We derive a closed form expression for the magnetic field $h_c(r)$ generated by a N-loop air core solenoid with the radius ϱ and length l. In our development, the thickness of the coil is neglected, i.e., it is assumed that the outer radius of the solenoid is very close to its inner radius. When this assumption is not valid, a first approximation is to choose ϱ as the average of the inner and the outer radii. The solenoid axis is assumed to be along the z-axis of a xyz coordinate system such that the solenoid is extended from $z = 0$ toward $z = -l$. We first determine the magnetic field $h_{3D}(x, y, z)$, $z > 0$ in three dimension and then compute $h_c(r)$ in the two-dimensional xz plane according to

$$h_c(r) = h_c(r_1, r_2) = \begin{bmatrix} 0 & 0 & 1 \\ 1 & 0 & 0 \end{bmatrix} h_{3D}(r_2, 0, r_1). \tag{42}$$

Let $h^s_{3D}(x, y, z)$ be the magnetic field due to a unit electrical current passing through a single loop of the solenoid in the xy plane. Then, by the linearity of Maxwell's equations, the total magnetic field due to a N-loop solenoid can be expressed as

$$h_{3D}(x, y, z) = \sum_{k=0}^{N-1} h^s_{3D}(x, y, z + lk/N).$$

This sum can be approximated by an integral according to

$$\begin{aligned} h_{3D}(x, y, z) &= \frac{N}{l} \sum_{k=0}^{N-1} h^s_{3D}(x, y, z + lk/N) \frac{l}{N} \\ &\simeq \frac{N}{l} \int_0^l h^s_{3D}(x, y, z + u)\, du \\ &= N \int_0^1 h^s_{3D}(x, y, z + lv)\, dv. \end{aligned} \tag{43}$$

We use the Biot-Savart [17] law in order to determine the magnetic field due to a single loop. This law describes the magnetic field due to a differential element $d\ell$ of a wire according to

$$dh^s_{3D} = \frac{\mu_0}{4\pi} \cdot \frac{d\ell \times s}{\|s\|^3} \tag{44}$$

where μ_0 is the permeability of free-space, s is the displacement vector from the wire element to the point at which the field is being computed, and dh^s_{3D} is the differential contribution of $d\ell$ to the total magnetic field. Let P be a point on the loop and θ be the angle between P and the x-axis. Then, $d\ell$ and s can be represented as

$$\begin{aligned} d\ell &= (-\varrho \sin\theta d\theta, \varrho \cos\theta d\theta, 0) \\ s &= (x - \varrho\cos\theta, y - \varrho \sin\theta, z). \end{aligned}$$

Applying these results to (44) and integrating over $\theta = [0, 2\pi]$, we get

$$h^s_{3D}(x, y, z) = \frac{\mu_0 \varrho}{4\pi} \int_0^{2\pi} \frac{(z\cos\theta, z\sin\theta, \varrho - x\cos\theta - y\sin\theta)\, d\theta}{\|(x - \varrho\cos\theta, y - \varrho\sin\theta, z)\|^3}.$$

Substituting this result into (43), we obtain the total magnetic field $h_{3D}(x, y, z)$ which is combined with (42) to obtain

$$h_c(r) = \frac{\mu_0 N \varrho}{4\pi} \int_0^1 \int_0^{2\pi} \frac{(\varrho - r_2\cos\theta, (r_1 + lv)\cos\theta)\, d\theta\, dv}{\|(r_2 - \varrho\cos\theta, \varrho\sin\theta, r_1 + lv)\|^3}.$$

With some efforts, we can simplify this expression to

$$h_c(r) = k \begin{bmatrix} \beta_1(r/\varrho) - \beta_1(r/\varrho + \nu) \\ \beta_2(r/\varrho) - \beta_2(r/\varrho + \nu) \end{bmatrix} \tag{45}$$

where $k = \mu_0 N/4\pi l$, $\nu = [l/\varrho \quad 0]^T$, and $\beta_1(\cdot)$ and $\beta_2(\cdot)$ are defined as

$$\begin{aligned} \beta_1(r) &= \int_0^{2\pi} \frac{r_1}{(r_2 - \cos\theta)^2 + \sin^2\theta} \\ &\qquad \times \frac{(r_2\cos\theta - 1)\, d\theta}{\left(r_1^2 + (r_2 - \cos\theta)^2 + \sin^2\theta\right)^{1/2}} \\ \beta_2(r) &= \int_0^{2\pi} \frac{\cos\theta\, d\theta}{\left(r_1^2 + (r_2 - \cos\theta)^2 + \sin^2\theta\right)^{1/2}}. \end{aligned}$$

For every fixed r, these functions can be computed by means of numerical integration.

The electromagnets used in our testbed are iron core rather than air core solenoids, thus (45) is not an exact description for the magnetic field of the electromagnets. However, our direct measurement of the magnetic field indicates a reasonably close match between (45) and the empirical data, particularly for points not very close to the face of the solenoid. In fact, with an acceptable approximation, the effect of the iron core is to increase the value of the coefficient k without drastically changing the shape of the field. We have determined the optimal value of k from the empirical data by solving a least squares problem. An alternative for this approximate model is to numerically solving Maxwell's equations using a computer software.

ACKNOWLEDGMENT

The authors would like to thank Z. Cummins, J. Lin, and R. Probst for contributing to the experiment design and operation.

REFERENCES

[1] A. H. B. de Vries, B. E. Krenn, R. van Driel, and J. S. Kanger, "Micro magnetic tweezers for nanomanipulation inside live cells," *Biophys. J.*, vol. 88, pp. 2137–2144, Mar. 2005.

[2] B. G. Hosu, K. Jakab, P. Bánki, F. I. Tóth, and G. Forgacs, "Magnetic tweezers for intracellular applications," *Rev. Scientif. Instrum.*, vol. 74, pp. 4158–4163, Sep. 2003.

[3] F. J. Alenghat, B. Fabry, K. Y. Tsai, W. H. Goldmann, and D. E. Ingber, "Analysis of cell mechanics in single vinculin-deficient cells using a magnetic tweezer," *Biochem. Biophys. Res. Commun.*, vol. 277, no. 1, pp. 93–99, 2000.

[4] J. S. Kanger, V. Subramaniam, and R. van Driel, "Intracellular manipulation of chromatin using magnetic nanoparticles," *Chromosome Res.*, vol. 16, pp. 511–522, May 2008.

[5] M. A. M. Gijs, F. Lacharme, and U. Lehmann, "Microfluidic applications of magnetic particles for biological analysis and catalysis," *Chem. Rev.*, vol. 110, no. 3, pp. 1518–1563, 2010.

[6] U. Lehmanna, S. Hadjidja, V. K. Parashara, C. Vandevyverb, A. Ridaa, and M. A. M. Gijs, "Two-dimensional magnetic manipulation of microdroplets on a chip as a platform for bioanalytical applications," *Sensors Actuators B: Chem.*, vol. 117, pp. 457–463, Oct. 2006.

[7] U. Schillingera, T. Brilla, C. Rudolphb, S. Huthb, S. Gerstingb, F. Krötzc, J. Hirschbergerd, C. Bergemanne, and C. Plank, "Advances in magnetofection—magnetically guided nucleic acid delivery," *J. Magnet. Magnet. Mater.*, vol. 293, pp. 501–508, May 2005.

[8] R. F. Probstein, *Physicochemical Hydrodynamics: An Introduction*, 2nd ed. New York: Wiley, 1994.

[9] C. I. Mikkelsen, "Magnetic separation and hydrodynamic interactions in microfluidic systems," Ph.D. dissertation, Dept. Micro Nanotechnol., Techn. Univ. Denmark, Lyngby, 2005.

[10] C. Gosse and V. Croquette, "Magnetic tweezers: Micromanipulation and force measurement at the molecular level," *Biophys. J.*, vol. 82, pp. 3314–3329, Jun. 2002.

[11] F. Amblard, B. Yurke, A. Pargellis, and S. Leibler, "A magnetic manipulator for studying local rheology and micromechanical properties of biological systems," *Rev. Scientif. Instrum.*, vol. 67, pp. 818–827, Mar. 1996.

[12] S. Tamaz, R. Gourdeau, and S. Martel, "Bidimensional MRI-based navigation system using a PID controller," in *Proc. 28th IEEE EMBS Annu. Int. Conf.*, 2006, pp. 4424–4427.

[13] F. M. Creighton, "Control of magnetomotive actuators for an implanted object in brain and phantom materials," Ph.D. dissertation, Dept. Phys., Univ. Virginia, Charlottesville, 1991.

[14] D. C. Meeker, E. H. Maslen, R. C. Ritter, and F. M. Creighton, "Optimal realization of arbitrary forces in a magnetic stereotaxis system," *IEEE Trans. Magn.*, vol. 32, no. 3, pp. 320–328, Mar. 1996.

[15] A. Komaee and B. Shapiro, "Steering a ferromagnetic particle by magnetic feedback control: Algorithm design and validation," in *Proc. Amer. Control Conf.*, 2010, pp. 6543–6548.

[16] R. Probst, J. Lin, A. Komaee, A. Nacev, Z. Cummins, and B. Shapiro, "Planar steering of a single ferrofluid drop by optimal minimum power dynamic feedback control of four electromagnets at a distance," *J. Magnet. Magnet. Mater.*, vol. 323, pp. 885–896, Apr. 2011.

[17] R. P. Feynman, R. B. Leighton, and M. Sands, *The Feynman Lectures on Physics*. San Francisco, CA: Pearson/Addison-Wesley, 2006.

[18] C. A. Desoer and E. S. Kuh, *Basic Circuit Theory*. New York: McGraw-Hill, 1969.

[19] Q. A. Pankhurst, J. Connolly, S. K. Jones, and J. Dobson, "Applications of magnetic nanoparticles in biomedicine," *J. Phys. D: Appl. Phys.*, vol. 36, pp. R167–R181, Jun. 2003.

[20] K. Ogata, *Modern Control Engineering*, 4th ed. Upper Saddle River, NJ: Prentice-Hall, 2002.

[21] R. C. Dorf and R. H. Bishop, *Modern Control Systems*, 11th ed. Upper Saddle River, NJ: Pearson/Prentice-Hall, 2008.

[22] W. J. Rugh, *Linear System Theory*, 2nd ed. Englewood Cliffs, NJ: Prentice-Hall, 1996.

[23] H. K. Khalil, *Nonlinear Systems*, 2nd ed. Upper Saddle River, NJ: Prentice-Hall, 1996.

[24] *Nonlinear Process Control*, M. A. Henson and D. E. Seborg, Eds. Upper Saddle River, NJ: Prentice-Hall, 1997.

[25] P. J. Campo, "Studies in robust control of systems subject to constraints," Ph.D. dissertation, Dept. Chem. Eng., California Inst. Technol., Pasadena, 1990.

[26] R. D. Braatz, M. L. Tyler, M. Morari, F. R. Pranckh, and L. Sartor, "Identification and cross-directional control of coating processes," *AIChE J.*, vol. 38, pp. 1329–1339, Sep. 1992.

[27] D. S. Bernstein, *Matrix Mathematics: Theory, Facts, and Formulas With Application to Linear Systems Theory*. Princeton, NJ: Princeton Univ. Press, 2005.

[28] D. L. Ma, S. H. Chung, and R. D. Braatz, "Worst-case performance analysis of optimal batch control trajectories," *AIChE J.*, vol. 45, pp. 1469–1476, Jul. 1999.

[29] Z. K. Nagy and R. D. Braatz, "Worst-case and distributional robustness analysis of finite-time control trajectories for nonlinear distributed parameter systems," *IEEE Trans. Control Syst. Technol.*, vol. 11, no. 5, pp. 694–704, Sep. 2003.

[30] P. C. Hansen, *Rank-Deficient and Discrete Ill-Posed Problems: Numerical Aspects of Linear Inversion*. Philadelphia, PA: SIAM, 1998.